## PAPER

# meso-Carbazole decorated BODIPYs – an electron donor–acceptor system with excellent fluorosolvato/vapochromic behavior, aggregation-induced emission, and antileishmanial activity†

Diana Mathew,[ac] Santanu Sasidharan,[b] Prakash Saudagar,[b] Subramaniam Sujatha*[a] and Pattiyil Parameswaran ⓘ *[c]

We report the synthesis and photophysical properties of meso-carbazole BODIPY **C1** and its β-mono-bromo (**C2**) and β,β′-dibromo (**C3**) substituted derivatives. Since carbazole is electron-rich as compared to BODIPY, the compounds **C1** and **C2** act as electron donor–acceptor systems and show red-shifted fluorosolvato/vapochromism with a Stokes shift of 170–180 nm as the dielectric constant of the solvent increases. This fluorosolvato/vapochromism is attributed to twisted intramolecular charge transfer (TICT), as confirmed by viscosity-dependent studies. The fluorescence emission and solvent polarity-dependent fluorochromism are hardly observed in the dibromo derivative **C3** due to the enhanced intersystem crossing (ISC), which is evident from DPBF titrations and the molecular orbital analysis. All three luminogens show excellent aggregation-induced emission (AIE) behavior and act as red-light-emitting aggregates. Thus, the low-intensity TICT-induced red emission can be enhanced by aggregate formation. Moreover, here we report for the first time the anti-leishmanial activity of carbazole BODIPYs against *Leishmania donovani* promastigotes, which can be taken forward as potential anti-leishmanial compounds.

## Introduction

Organic luminescent materials have received multifaceted interest in scientific and technological fields due to their potential applications as light-harvesting devices,[1] tunable organic laser dyes,[2] fluorescent sensors,[3] biological labeling and imaging dyes.[4–6] Among them, the boron dipyrromethene (BODIPY) fluorescent dyes have been the focus of considerable research over the last three decades.[7] Their photophysical properties can be modified by the nature of the substituents and their position on the BODIPY core. Moreover, the functionalized derivatives, such as halogenated BODIPYs, are key

building blocks for synthesizing substituted BODIPYs. Indeed, they generate longer wavelength BODIPY dyes and are potential sensitizers for photodynamic therapy (PDT).[8,9] Thus, the effect of halogen atoms such as bromine on the structural and spectral properties of BODIPYs is quite interesting.[10–12]

Although the structural versatility of BODIPYs benefits tuning their photophysical and chemical properties,[11] the major challenge in applying this family of dyes is the aggregation caused quenching (ACQ) in their solid-state and small Stokes shift of the α,β-unsubstituted derivatives.[13] One approach to achieving a large Stokes shift is to incorporate electron-rich moieties at the meso-position of BODIPYs selectively. This will induce a charge transfer process and exhibit excellent solvatochromic and vapochromic luminescence effects.[16–18] However, the solvent polarity-dependent red-shifted emission is usually weakened in solution due to intramolecular charge transfer (ICT). On the other hand, the red emission can be revived by the formation of aggregates. Restricting intramolecular motion in the aggregates enhances the luminance efficiency in the condensed state (aggregation-induced emission (AIE)).[14,15] Hence, appending bulky groups at the BODIPY core is suitable for generating twisted structures, which hampers the π–π interactions between the adjacent molecules.

[a] Department of Chemistry, Bioinorganic Materials Research Laboratory, National Institute of Technology Calicut, Kozhikode, 673 601, India. E-mail: ssinorgsuji@gmail.com

[b] Department of Biotechnology, National Institute of Technology Warangal, Warangal, 506004, India

[c] Department of Chemistry, Theoretical and Computational Chemistry Laboratory, National Institute of Technology Calicut, Kozhikode, 673 601, India. E-mail: param@nitc.ac.in

Hence, we have selected the carbazole unit, which has an electron-rich and bulky aromatic fragment, having good absorption and photoluminescence behavior for the construction of a donor–acceptor system.[19–21] Carbazole is known for its unique properties such as excellent thermal and chemical stability, low redox potential, facile functionalization of the aromatic ring, hole transport properties, and medicinal activity.[22–24,33] It is reported that the absorption and emission behavior of BODIPYs can be modified by the presence of an electron-rich carbazole moiety.[25,26] The linkage and the position at which carbazole is attached to the BODIPY scaffold play a major role. The structural diversity of the carbazole-BODIPY conjugates includes the BODIPY derivatives with carbazole rings at the *alpha*, *beta*, and *meso*-positions of the BODIPY skeleton.[27–32,38] Recently, Kesavan et al. reported that the carbazole at the *meso*-position altered the electronic properties of the BODIPYs.[28] Misra et al. studied the donor–acceptor interactions between carbazole and BODIPY,[34] while Giribabu and coworkers described the photoinduced energy transfer in carbazole-BODIPY dyads.[25] Though the reports on carbazole-substituted BODIPYs have increased considerably, an unambiguous report of the AIE effect of carbazole-BODIPYs is not yet reported.

Considering the unique photophysical properties of carbazole, we combined BODIPY with carbazole to design an electron donor–acceptor system with dual photoresponse to solvent polarity and luminogen aggregation. The red-shifted and quenched emission in polar solvents caused by TICT can be revived by the AIE behavior of *meso*-carbazole BODIPYs in aqueous mixtures. We further discuss the role of bromine substitution in generating triplet photosensitizers.

The details of the antileishmanial activity of BODIPY dyes are very limited in the literature. Leishmaniasis is an intracellular protozoal parasitic infection that causes a spectrum of diseases in humans. Leishmaniasis remains in the cutaneous form to the fatal visceral form worldwide because of the unavailability of safe and cost-effective drugs for treatment. Inspired by the reports on the antileishmanial activity of carbazole-based compounds,[35–37] we attempted antileishmanial studies of the synthesized carbazole-BODIPY derivatives towards *Leishmania donovani* promastigotes.

## Results and discussion

### Syntheses and characterization of *meso*-carbazole BODIPY and its brominated derivatives

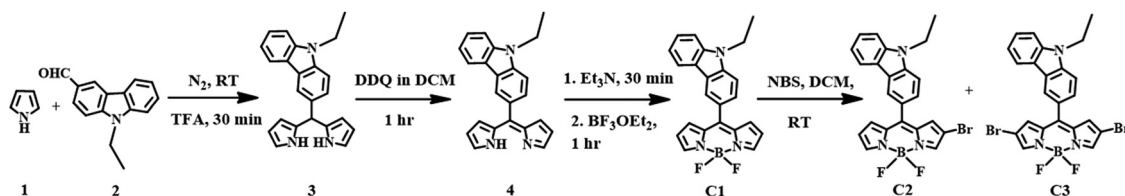The *meso*-carbazole substituted BODIPY (**C1**) was synthesized in a one-pot reaction, which involves the synthesis of dipyrromethane (**3**) followed by oxidation with 3-dichloro-5,6-dicyano-1,4-benzoquinone (DDQ) and further complexation with borontrifluoroetherate (BF$_3$OEt$_2$) (Scheme 1). The *meso*-carbazole appended dipyrromethane (**3**) was obtained by trifluoroacetic acid (TFA)-assisted condensation between pyrrole (**1**) and N-ethyl carbazole-3-carboxaldehyde (**2**) as per the literature.[11,21]

The dipyrromethane formed was immediately subjected to oxidation with DDQ in DCM at room temperature for an hour after removing the excess pyrrole. The resulting dipyrrin (**4**) was complexed with BF$_3$OEt$_2$. The reaction was achieved within an hour, and the corresponding *meso*-carbazole appended BODIPY (**C1**) was isolated by silica gel column chromatography as a reddish-orange powder with a 35% yield.

The regioselective bromination of α,β-unsubstituted BODIPY **C1** was done by the reaction with N-bromosuccinimide (NBS) in two different equivalences (Scheme 1).[39,40] The treatment of **C1** with 1.2 equivalents of NBS resulted in the formation of 75% **C2** along with unreacted **C1**. However, the addition of 2.4 equivalents gave 25% **C3** along with a 15% yield of **C2**.

The synthesized *meso*-carbazole BODIPY derivatives were quite soluble in common organic solvents and were characterized by FTIR, $^1$H, and $^{13}$C NMR spectroscopic methods, high-resolution mass spectrometry (HRMS), and XRD analysis, as well as by UV-visible and fluorescence spectroscopic techniques. The IR spectra of the synthesized compounds show the characteristic aromatic =C–H vibrational peak at 2923 cm$^{-1}$ and the vibrational peak at 1537 and 1735 cm$^{-1}$ corresponding to B–F and C=N stretching in the BODIPY core (Fig. S1, ESI†). The B–N stretching frequency is observed at 1068 cm$^{-1}$. The strong vibrations around 1342–1266 cm$^{-1}$ correspond to the C–N stretching of the carbazole moiety. The β-C–H stretching vibration of the pyrrole ring observed at 770 cm$^{-1}$ in unbrominated BODIPY **C1** is absent in the brominated derivative **C3**. The absorption in the range of 500–600 cm$^{-1}$ indicates the presence of the C–Br stretching frequency of aryl bromides in brominated BODIPYs **C2** and **C3**.

In the $^1$H NMR spectra of the synthesized BODIPYs, the proton intensities and chemical shifts agree with the expected structure. The $^1$H NMR spectra of BODIPY **C1** show two peaks of two proton intensities at δ 6.57 ppm and δ 7.04 ppm, which corresponds to two sets of β-pyrrolic hydrogens and the α-pyrrolic protons appear as a singlet at δ 7.94 ppm (Fig. S2, ESI†). The carbazole aromatic protons appear as five sets of signals between δ 7.31 and δ 8.35 ppm. The N-ethyl aliphatic protons appear as a triplet of three hydrogen intensities at δ



**Scheme 1** Synthesis of *meso*-carbazole substituted BODIPY (**C1**) and its mono- (**C2**) and dibromo derivatives (**C3**).

1.52 ppm and a quartet of two hydrogen intensities at $\delta$ 4.46 ppm. The absence of proton signals corresponding to β-pyrrole hydrogens at the 2- and 2,6-positions indicates the successful bromination at the β-pyrrole carbon in **C2** and **C3**, respectively (Fig. S2b and S2c, ESI†). The $^{13}$C NMR spectra of BODIPYs **C1–C3** recorded in CDCl$_3$ show peaks at $\delta$ 148.1, 146.1, 145.2, 141.1 ppm, corresponding to the aromatic pyrrolic carbon signals. The aromatic carbazole peaks appear between $\delta$ 133.3 and $\delta$ 103.7 ppm. The two aliphatic carbon atoms of the N-ethyl substituent at the carbazole unit appear around $\delta$ 14.1 and $\delta$ 39.5 ppm in the $^{13}$C NMR spectra of the BODIPYs (Fig. S3, ESI†). The mass spectrum of the compounds discloses the peak representing the molecular ion at $m/z$ = 385.1573, 465.0664, and 542.9751, for **C1**, **C2**, and **C3**, which represents the protonated molecular ion (Fig. S4, ESI†).

### Single crystal X-ray diffraction studies

The single crystal of the BODIPY **C1** was obtained by the slow evaporation of hexane into chloroform for two weeks. The BODIPY **C1** crystallizes in a monoclinic crystal system with a P2$_1$/c space group (Fig. 1a and Tables S1, S2, ESI†). The two pyrrole rings and the boron-containing central six-membered ring are coplanar ($\Phi_{\text{pyrrole}}$ = 178.5°), while fluorine atoms are in different planes. The boron atom in BODIPY **C1** exhibits distorted tetrahedral geometry with an N1–B–N2 angle of 106.0° and F1–B–F2 angle of 108.5° (F1–B–N1 = 110.16°).

The dihedral angle between the *meso*-carbazole substituent and the BODIPY core is midway between planar and perpendicular conformation. This non-planar arrangement of *meso*-carbazole substituent with the BODIPY core limits the possible resonance between the BODIPY core and the carbazole substituent, which is confirmed by the presence of C$_{\text{BODIPY}}$–C$_{\text{Carbazole}}$ single-bond distance (1.472 Å). The molecular crystal packing of **C1** exhibits a parallel 3D arrangement of molecules stabilized by (BODIPY)B⋯H–C(carbazole) interaction (B1–H10 = 3.008 Å), (pyr)C⋯C(carbazole) π–π interactions (C13–C10 = 3.345 Å, C14–C10 = 3.368 Å) and (BODIPY)F⋯H–C(carbazole)

intermolecular hydrogen bonding interactions (F2–H10 = 2.633 Å, F1–H3 = 2.669 Å, F1–H22 = 2.562 Å, F2–H9 = 2.576 Å) (Fig. 1b and c).

### Photophysical properties

The photophysical properties of carbazole and the synthesized compounds were studied in solvents of different polarities and tabulated in Tables S3, and S4 (ESI†). The aromatic π → π* transitions of the carbazole chromophore are attributed to the peaks at 293, 333, and 342 nm (Fig. 2).[25,26] The synthesized *meso*-carbazole substituted BODIPY **C1–C3** shows a well-resolved and intense absorption band in the 490–535 nm region with a shoulder centered around 480 nm and a weak broad absorption band around ∼330–390 nm.

Introducing a carbazole moiety at the *meso*-position of the BODIPY chromophore did not cause any drastic spectral change in the UV-vis spectra compared to *meso*-phenyl BODIPY except for a peak around 290 nm in the UV region corresponding to the carbazole unit. This is due to the non-planar arrangement of the *meso*-carbazole substituent with the aromatic BODIPY core, which prevents electron π-conjugation, which is evident in the crystal structure. On the other hand, the substitution of bromine at the pyrrole carbon produced a redshift of ∼10 nm in the $\lambda_{\text{max}}$, which is consistent with the reported literature.[11] The $\lambda_{\text{max}}$ is red-shifted from 499 nm in **C1** to 516 nm in **C2** in hexane, and is further shifted to 533 nm in dibromo derivative **C3** (Fig. S5a, ESI†).

The fluorescence analysis of *meso*-carbazole substituted BODIPYs shows that **C1** gives an emission at 507 nm in hexane ($\lambda_{\text{exc}}$ = 480 nm) (Fig. S5b, ESI†). A significant red-shift of ∼20 nm was observed in the emission maximum through each attached bromine in brominated derivatives **C2** ($\lambda_{\text{max}}$ = 527 nm) and **C3** ($\lambda_{\text{max}}$ = 549 nm), along with a decrease in fluorescence quantum yield. The fluorescence quantum yield in hexane decreased from 0.51 (**C1**), to 0.4 (**C2**) to 0.11 (**C3**) in unbrominated and brominated derivatives, owing to the heavy halogen effect, which was more prominent in dibromo derivative **C3**.[11]
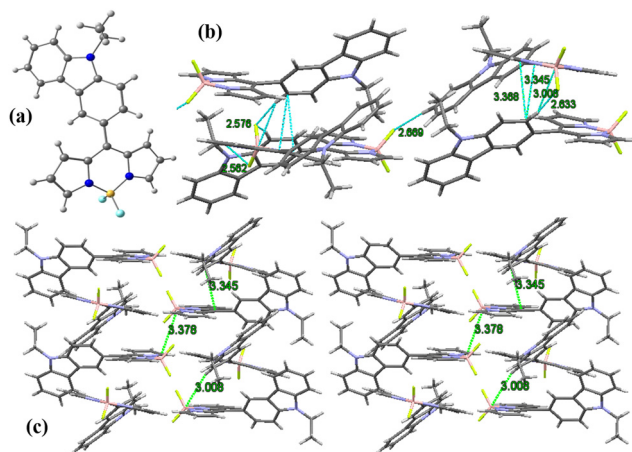


Fig. 1 (a) X-Ray crystal structure of BODIPY **C1**; (b) unit cell and intermolecular interactions in **C1**; (c) molecular crystal packing of BODIPY **C1**.
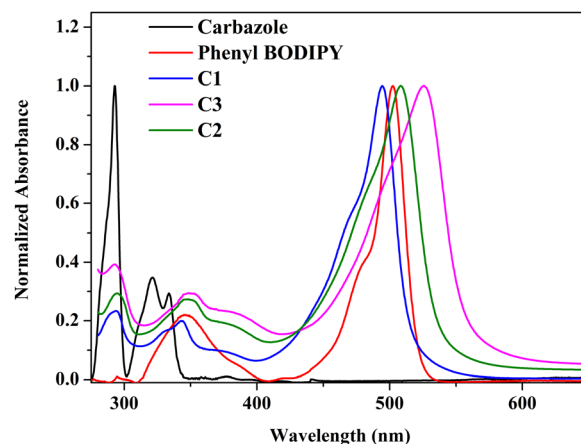


Fig. 2 Normalized absorption spectra of carbazole, phenyl-BODIPY, and *meso*-carbazole BODIPYs–**C1**, **C2** and **C3** in hexane ($10^{-5}$ M) at room temperature.

The synthesized *meso*-carbazole substituted BODIPYs **C1** and **C2** show remarkable fluorosolvatochromism (*vide infra*). Hence, the fluorescence efficiency of the BODIPY can be modulated by incorporating the carbazole unit at the *meso*-position.

The BODIPYs **C1**, **C2**, and **C3** are strongly emissive in their solid state. The emission peaks are observed at 626, 597, and 620 nm for **C1**, **C2**, and **C3** (Fig. S5c, ESI†). The placement of the bulky carbazole group on the BODIPY core structure hinders π–π stacking between the neighboring molecules and enhances the emission in the solid state. The solid-state spectrum of the compounds shows notable emission at a longer wavelength, as expected, considering the stronger intermolecular interactions.[49]

**Theoretical calculations**

We have performed quantum mechanical calculations to understand the structural and electronic properties of the synthesized *meso*-carbazole-substituted BODIPYs. The geometrical optimizations were carried out in the gas phase by choosing the initial coordinates from the X-ray crystallography data (Fig. 3).

The geometrical parameters of **C1** agree with the single-crystal data. The carbazole ring and the BODIPY core are non-planar to each other (dihedral angle between the carbazole and BODIPY plane $\Phi_{carb}$ = 51°) and the bromine substitution at the β-pyrrolic carbon does not yield a significant geometrical change. The β-pyrrolic carbon atoms of BODIPY **C1** are comparatively nucleophilic, which validates well the molecular electrostatic potential (MESP) values on the van der Waals surface of the carbon atoms (Fig. S6, ESI†). The MESP values on the β-pyrrolic carbon atom C24 ($-10.04$ kcal mol$^{-1}$) have more negative potential as compared to the carbazole carbon atoms C2, C13, and C18 ($-4.50$, $-0.89$, and $-3.66$ kcal mol$^{-1}$, respectively) (Table S5, ESI†). This explains the successful electrophilic bromination at β-pyrrolic carbon atoms other than at the carbazole ring.

The frontier molecular orbital analysis of **C1–C3** in the singlet state in DMSO shows that the highest occupied molecular orbital (HOMO) is mainly localized on the carbazole unit, and the lowest unoccupied molecular orbital (LUMO) is on the BODIPY core. The HOMO−1 orbital is localized on the

BODIPY core with the contribution from bromine in **C2** and **C3** (Fig. 4).

To study the electronic absorption behavior and the effect of solvents on the photophysical properties of the BODIPYs **C1–C3**, time-dependent density functional theory (TD-DFT) calculations were performed in DMSO using the PCM solvent model at the M06/Def2-TZVPP//BP86/Def2-TZVPP level of theory. The computed vertical transitions and their oscillator strengths directly correlate with the experimental results. The HOMO−1, HOMO, and LUMO molecular orbitals are mainly involved in the transitions. The most probable transition in DMSO is from HOMO−1 → LUMO in **C1** ($\lambda_{max}$ calc. = 427 nm, $f$ = 0.37), **C2** ($\lambda_{max}$ calc. = 444 nm, $f$ = 0.37), and **C3** ($\lambda_{max}$ calc. = 461 nm, $f$ = 0.41), which corresponds to π → π* transition in the BODIPY core (Table S6, ESI† and Fig. 4). There is one more transition at a higher wavelength having appreciable oscillator strength (**C1**: $\lambda_{max}$ calc. = 490 nm $f$ = 0.25, **C2**: $\lambda_{max}$ calc. = 508 nm $f$ = 0.26, and **C3**: $\lambda_{max}$ calc. = 526 nm $f$ = 0.27), which corresponds to the π → π* transition between the carbazole and the BODIPY and denotes a charge-transfer transition. Note that the oscillator strength of this transition is reduced considerably when the TDDFT calculations are performed on a structure with $\Phi_{carb}$ = 90° (Table S7 and Fig. S7, ESI†). This matches with the experimentally observed absorption spectra that the charge transfer is not observed in the ground state geometry. This is because the free rotation of carbazole with respect to the BODIPY core is possible between the dihedral angle 51° to 128.8° (51° and 128.8° are equivalent structures) through 90° as it can easily overcome the energy barrier of 1.46 kcal mol$^{-1}$ at room temperature (Fig. S21 – rotational energy plot, ESI†) (*vide infra*).

Moreover, the bromine substitution at the pyrrolic carbon has imparted stabilization in the molecular orbitals in **C2** and **C3**, and subsequently, the HOMO−1 → LUMO energy gap is reduced from 3.46 eV in **C1** to 3.38 eV in **C2** and 3.31 eV in **C3** (Fig. S8, ESI†). This explains the bathochromic shift in $\lambda_{max}$ observed in the absorption spectra upon bromination. These results indicate that the electronic structure of these compounds can be influenced by regioselective bromination, which can tune their photophysical properties.

**Intramolecular excitation energy transfer**

Intramolecular excitation energy transfer is observed in the *meso*-carbazole BODIPYs. The parameters such as solvent used, concentration, and slit width were kept constant in this study to compare the results at different emission wavelengths.

The excitation of *meso*-carbazole BODIPY at 290 nm in CHCl$_3$ results in the HOMO → LUMO+1 transition, where both orbitals are in the carbazole unit. Interestingly, the emission occurs from the BODIPY unit at 500 nm in **C1**, and the carbazole emission was significantly diminished in the spectra. Similarly, **C2** emits at 505 nm, and **C3** gives a weak emission at 513 nm upon excitation at 290 nm (Fig. 5a). The emission at 500 nm occurs from the LUMO → HOMO−1 orbital localized on the BODIPY core (Fig. 5b and Fig. S9, ESI†). Hence, the photophysical mechanism can be explained as follows. The S$_0$ → S$_2$ absorption occurs by the absorption of radiation
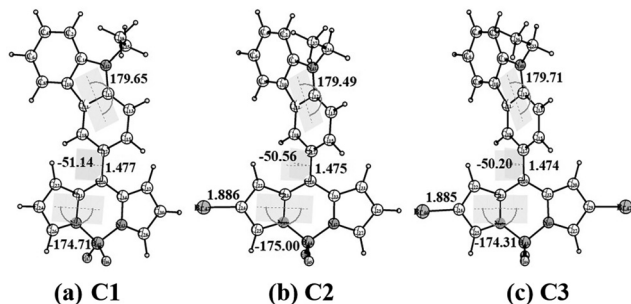


Fig. 3 Optimized geometry of *meso*-carbazole substituted BODIPY **C1**, **C2**, and **C3** at the BP86/def2-TZVPP level of theory at the ground state in the gas phase. All angles are given in degrees and bond lengths in Å.
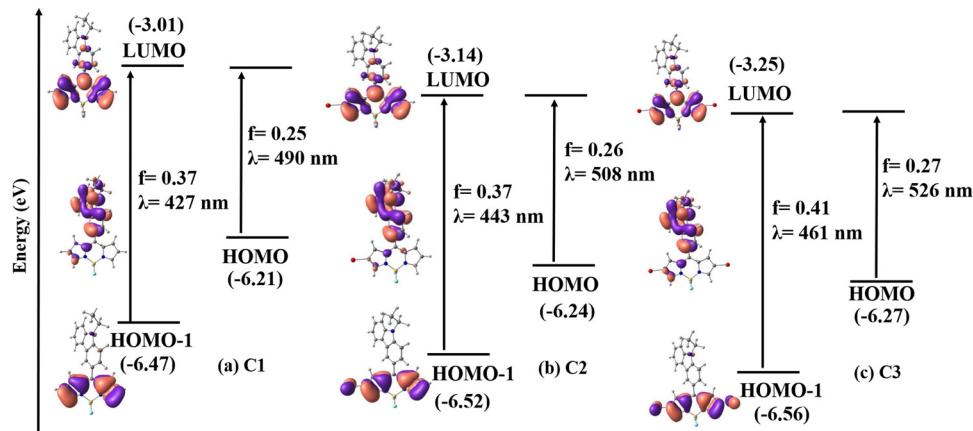
**Fig. 4** Selected molecular orbitals and important electronic transitions of **C1**, **C2**, and **C3** computed using TDDFT at the M06/def2-TZVPP//BP86/def2-TZVPP level of theory in DMSO using the PCM solvent model. Eigenvalues are given in eV. The surfaces are plotted at the iso-surface value of 0.03. The corresponding wavelength ($\lambda$) in nm and oscillator strength ($f$) are given.
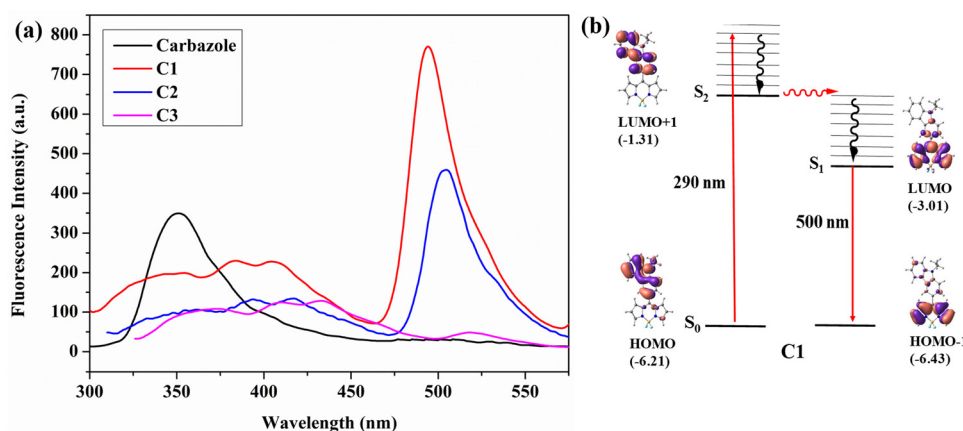


**Fig. 5** (a) Fluorescence spectrum of *meso*-carbazole substituted BODIPYs **C1**, **C2**, and **C3** ($10^{-7}$ M, $\lambda_{ex}$ = 290 nm) and carbazole ($10^{-7}$ M) in chloroform at room temperature; (b) important molecular orbitals and electronic transitions occurring in **C1** calculated using TDDFT at the M06/Def2-TZVPP//BP86/Def2-TZVPP level of theory. Eigenvalues are given in eV.

at 290 nm, which then undergoes internal conversion to the $S_1$ state and the emission occurs from the $S_1$ state. These findings are consistent with the energy transfer efficiency calculated in carbazole BODIPY by Gupta *et al.*[21]

**Effect of solvents on photophysical properties of *meso*-carbazole BODIPYs**

The absorption and emission properties of the compounds were studied in solvents of different polarities (Tables S3 and S4, ESI†). The compounds **C1**, **C2**, and **C3** showed similar absorption profiles in solvents of different polarities (Fig. 6a). This indicates that the ground state dipole moment is not affected by solvent polarity. In contrast, the emission spectra of the compounds show strong solvent polarity dependence (Fig. 6b and Fig. S10, ESI†). In non-polar solvents like hexane, the emission band is structured and has a mirror-image relationship with their absorption spectra. This is because of the similar geometries of the absorbing and emitting species in

the non-polar solvents,[41] and the emission occurs from the $S_1$ state (LUMO → HOMO−1 transition). As the solvent polarity increased, the fluorescence band became broadened and red-shifted. The compound **C1** in hexane exhibited emission at 507 nm, with a fluorescence quantum yield ($\Phi_f$) of 0.51 (Fig. 7a and Table S4, ESI†). In THF, a broad and red-shifted peak is formed at 607 nm with a fluorescence quantum yield of 0.21.

Dual emission is observed in highly polar solvents like DMSO and methanol, which are weakened in intensity with $\Phi_f < 0.1$. A new red-shifted emission band is observed at 675 nm for **C1** in DMSO (LUMO → HOMO transition), attaining a Stokes shift of 182 nm. This is a characteristic of the twisted intramolecular charge transfer (TICT) effect[42,43] in BODIPYs, where the emission happens from two different states. Similar behaviour is observed for mono-bromo derivative **C2**, which also produces a solvent-dependent emission (Fig. S10b and S11a, ESI†). The emission wavelength is red-shifted by nearly 168 nm, from 527 nm in hexane to 676 nm in DMSO, and the
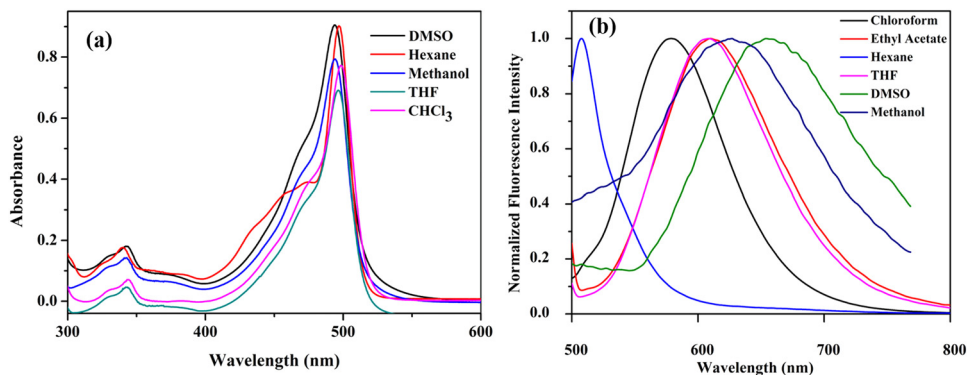
Fig. 6 (a) UV-visible spectrum ($10^{-5}$ M) and (b) fluorescence spectrum ($10^{-7}$ M, $\lambda_{ex}$ = 480 nm) (normalized) of **C1** in various solvents at room temperature.

fluorescence quantum yield decreased from 0.4 in hexane to 0.01 in DMSO (Table S4, ESI†). The fluorescence quenching efficiency, $Q$, can be estimated from the fluorescence quantum yield of carbazole ($\Phi_{(reference)}$) and the fluorescence quantum yield of BODIPY ($\Phi_{(BODIPY)}$) (Tables S3 and S4, ESI†), which increases with solvent polarity.[25]

The relationship between the dielectric property of the solvent and the corresponding Stokes shift for **C1**, **C2**, and **C3** was studied (Fig. 7b and Fig. S12, ESI†). For **C1** and **C2**, the Stokes shift shows an exponential increase with the dielectric constant of the solvent. The dielectric constant of non-polar solvents is almost proportional to the Stokes shift. Furthermore, as the dielectric constant increases with increasing solvent polarity, there is a sharper increase in the Stokes shift. This is because the dielectric properties of the polar environment strongly affect the charge transfer processes. No such correlation is observed for dibromo derivative **C3** (Fig. S12b, ESI†).

For a better understanding of the solvatochromic behavior, the fluorescence lifetimes ($\tau$) of these dyes were measured in solvents of different polarities (Tables S4 and S8, ESI†). They were best fitted with a biexponential function with a lifetime in the nanosecond range. Fitted decay time ($\tau_i$), pre-exponential coefficients ($\alpha_i$), and chi-squared ($\chi^2$) values and residuals are given in Table S8 and Fig. S13 (ESI†). The fluorescence lifetime gradually increases with increasing solvent polarity for **C1** (0.2 ns in hexane, 3.14 ns in DMSO) and **C2** (0.147 ns in hexane, 2 ns in DMSO), which confirms the excited state stabilization in polar solvents (Fig. 7c and Fig. S13a, ESI†). Furthermore, the radiative ($k_r$) and nonradiative ($k_{nr}$) decay rates[51] calculated from $\Phi_f$ and $\tau$ indicate that the radiative decay rate decreases sharply with increasing solvent polarity for both **C1** and **C2** (Table S4, ESI†). This strongly suggests that the decrease in fluorescence quantum yield is due to the nonradiative relaxation in polar solvents.
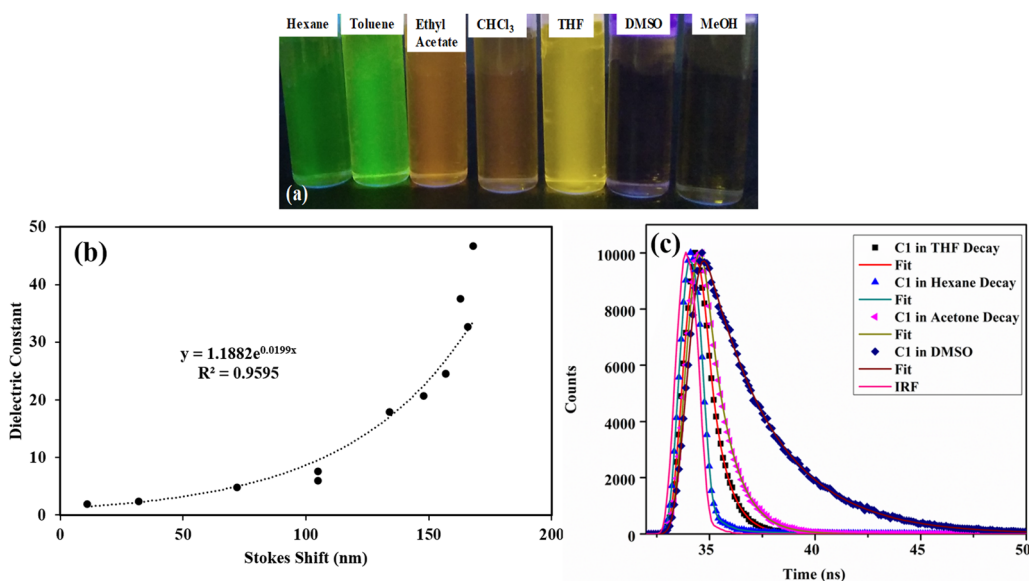


Fig. 7 (a) Photograph of **C1** in various solvents under UV irradiation-solvatochromism; (b) the plot of the dielectric constant *vs.* Stokes shift (nm) for **C1**; (c) the fluorescence decay profiles of **C1** in different solvents. The instrument response function (IRF) is shown in the red line.

The *meso*-carbazole substituted BODIPY **C1** and the mono-bromo derivative **C2** exhibit superior solvatochromic fluorescence features. While the dibromo derivative **C3** is non-emissive in all solvents with a small Stokes shift, no notable solvatochromism is observed (Fig. S10c, S11b, S12b and Table S4, ESI†). Moreover, the fluorescence lifetime is shorter for **C3** and not dependent on solvent polarity (0.65 in hexane, 0.61 in DMSO) (Fig. S13b, ESI†).

### Solvatochromic analysis for the estimation of the excited-state dipole moments

The sensitivity of the fluorophores to solvent polarity is studied in terms of the difference in the dipole moment between the ground and excited states. The solvent polarity-dependent increase in Stokes shift proposes an increase in the dipole moment upon excitation. This can be estimated from the Lippert–Mataga plot, which is the plot of Stokes shift ($\Delta\nu$) *versus* orientational polarizability ($\Delta f$), which is given as follows:[47]

$$\nu_A - \nu_F = \Delta\nu = \frac{2}{hca_0^3}\left[\frac{(\varepsilon - 1)}{(2\varepsilon + 1)} - \frac{(\eta^2 - 1)}{(2\eta^2 + 1)}\right](\mu_e - \mu_g)^2$$

$$= \frac{2\Delta f}{hca_0^3}\Delta\mu^2$$

where $c$ is the velocity of light, $h$ is Planck's constant, $\mu_e - \mu_g$ is the dipole moment difference between the excited and the ground states, respectively ($\Delta\mu$), and $a_0$ is the radius of the Onsager cavity around the BODIPYs, which is considered as the sphere. The dielectric constant ($\varepsilon$) and refraction index ($\eta$) of the solvent are grouped as $\Delta f$, which is known as orientation polarizability. The radius of the Onsager cavity is calculated at the M06/Def2-TZVPP level of theory (Table 1). The ground-state dipole moment for the compounds was calculated from the optimized ground-state geometry at the BP86/Def2-TZVPP level of theory in the gas phase. For different solvents, the Stokes shift is fitted to a Lippert–Mataga relationship and the difference between the ground and excited-state dipole moments ($\Delta\mu$) was calculated from the slopes of Lippert–Mataga plots (Fig. 8). The linear correlation between the Stokes shift and the orientation polarizability of **C1** and **C2** suggests the higher polarization of the excited states than the ground states. There is a significant increase in the dipole moment in the excited state (Table 1), and the larger excited state dipole moment for both **C1** and **C2** (Fig. 8 and Fig. S14a, ESI†) reflects the charge transfer characteristics of these dyes in the excited state.

The direction of the dipole moment in the ground state is from the electron-rich carbazole to the electron-deficient
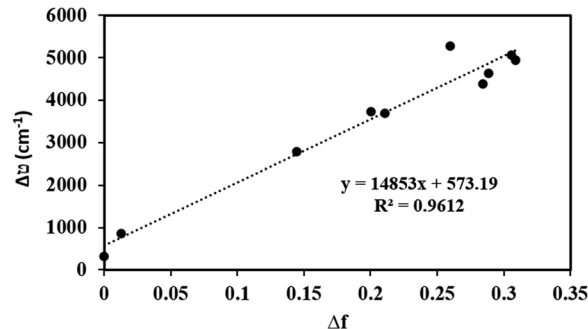


**Fig. 8** Lippert–Mataga plot: dependence of Stokes shifts on the solvent polarity function, $\Delta f$ for **C1**.

BODIPY core (Fig. S15, ESI†). The decreased value of the excited-state dipole moment for **C3** (Fig. S14b, ESI†) obtained from the Lippert–Mataga plot might be due to noticeable intersystem crossing due to the heavy atom effect.

### Twisted intramolecular charge transfer process

To verify the TICT in *meso*-carbazole BODIPY derivatives, we studied the solvent polarity and viscosity effect on the emission spectra. The solvent polarity was systematically varied by mixing the polar THF ($\varepsilon = 7.5$) and non-polar hexane ($\varepsilon = 1.8$) in different ratios and recording the emission spectra of the BODIPY derivatives (Fig. S16a, ESI†). In 100% THF, BODIPY **C1** has a red-shifted and broad emission at 627 nm. As the hexane fraction in the THF/hexane mixture is increased from 0 to 100%, the emission is blue-shifted and intensified. In 90% hexane, the peak in the longer wavelength region at 627 nm disappeared, and the sharp emission in the shorter wavelength region, $\sim 500$ nm became prominent. The effect of viscosity was examined in an ethanol ($\eta = 1.08$ cP)/glycerol ($\eta = 934$ cP) mixture (Fig. S16b, ESI†). There is dual emission observed in pure ethanol. The intensity of the emission band around 500 nm increases as the fraction of glycerol increases and the longer wavelength emission band completely disappeared in 100% glycerol.

The observed increase in emission at a higher wavelength with the decrease in viscosity and increase in polarity suggests that the charge transfer in the excited state is accompanied by a conformational change leading to the formation of a twisted intramolecular charge transfer (TICT) state. The non-polar or viscous environments prevent the rotation of the carbazole about the $C_{BODIPY}$–$C_{Carbazole}$ bond connected to the BODIPY unit.

Thus, in the non-polar/viscous solvent, the emission occurs from the $S_1$ state, giving a sharp emission band around 500 nm. In ethanol and THF, the intramolecular rotation brings the BODIPY to the TICT state, where the charge separation between the carbazole and BODIPY units occurs and obeys the minimum overlap rule.[58] The twisted molecular conformation is stabilized by the solvating effect of the polar solvent. Thus, the TICT emission is red-shifted and weakened (Scheme 2).

### Singlet oxygen generation: chemical quenching with DPBF

As discussed earlier, the non-emissive behavior of dibromo-BODIPY derivative **C3** can be anticipated to be due to the

**Table 1** Ground ($\mu_g$) and excited dipole moments ($\mu_e$) for **C1**, **C2**, and **C3**

| BODIPY | Onsager radius, $a_0$ (Å) calculated | $\mu_g$ (Debye) calculated | $\Delta\mu$ (Debye) from Lippert–Mataga plot | $\mu_e$ (Debye) = ($\Delta\mu + \mu_g$) |
|--------|------|------|------|------|
| C1 | 4.82 | 8.56 | 14.7 | 23.91 |
| C2 | 5.47 | 9.21 | 12.8 | 21.36 |
| C3 | 6.17 | 9.28 | 5.3 | 14.58 |
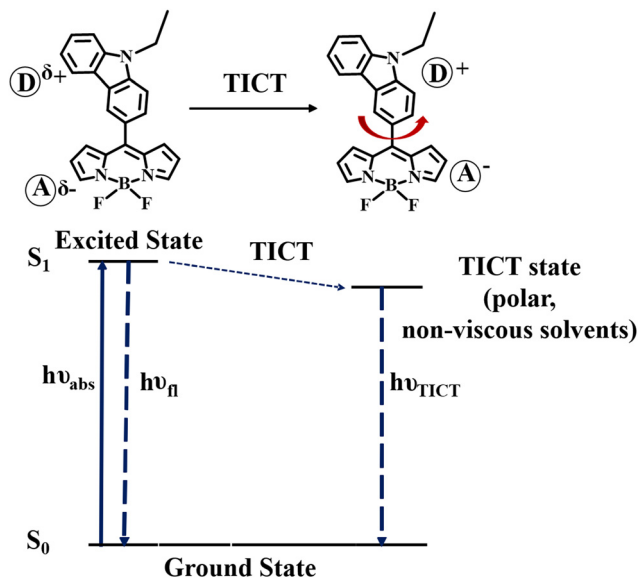
**Scheme 2** Schematic representation of TICT state formation in *meso*-carbazole BODIPY.

**Table 2** Calculated energy $\Delta E$ (kcal mol$^{-1}$) between the singlet and triplet states of O$_2$ and *meso*-carbazole substituted BODIPYs at the M06/Def2-TZVPP//BP86/Def2-TZVPP level of theory

| Compound | $\Delta E$ (kcal mol$^{-1}$) |
|---|---|
| $E(^1O_2) - E(^3O_2)$ | 37.21 |
| $E(T_1) - E(S_0)$ | |
| C1 | 38.52 |
| C2 | 38.27 |
| C3 | 37.57 |

intersystem crossing in **C3** produced by heavy atom bromine. The enhanced intersystem crossing in dibromo derivative **C3** is explained by calculating the singlet oxygen quantum yield by the chemical trapping method using diphenylisobenzofuran (DPBF) in DMSO.[44] The DPBF shows a faster degradation in the presence of the dibromo derivative than that of mono-bromo as well as unbrominated BODIPY (Fig. 9b). The steady degradation of DPBF occurs in the presence of singlet oxygen, generated by the dibrominated derivative in the triplet state as per the widely studied mechanism given in Fig. 9a.[45,46]

The singlet oxygen quantum yield is calculated using methylene blue as the reference and follows the order **C3** (0.48) > **C2** (0.23) > **C1** (0.15). The amount of $^1O_2$ produced is related to the population of BODIPY in the T$_1$ state. There are reports that molecules with charge transfer characteristics exhibit higher singlet oxygen quantum yield than those molecules without a charge transfer character.[61] As the solvent polarity is increased

in DMSO, the charge transfer is enhanced in **C1**, and the efficiency of **C1** for singlet oxygen generation is also increased significantly, resulting in a reasonable $^1O_2$ quantum yield of 0.15. However, the singlet oxygen quantum yield of unbrominated derivative **C1** is much less compared to dibromo derivative **C3**. Thus, incorporating heavy atom bromine at the 2,6-position of the BODIPY core could enhance the intersystem crossing (ISC), affectedly increase the singlet oxygen quantum yield, and decrease the fluorescence quantum yield in **C3**.

We calculated the energy difference between the singlet and triplet states of O$_2$ and *meso*-carbazole substituted BODIPY at the M06/Def2-TZVPP//BP86/Def2-TZVPP level of theory (Table 2). A correlation in the singlet–triplet energy gap is observed between the dioxygen and the compounds, though the energy difference among the compounds is minimal. The energy gap of dioxygen (37.21 kcal mol$^{-1}$) matches well with the energy difference between the triplet and singlet state of dibromo derivative **C3** (37.57 kcal mol$^{-1}$). The singly occupied molecular orbitals in the triplet state are SOMO and SOMO−1, which resulted from the excitation of an electron from the filled HOMO−1 orbital to the LUMO. The SOMO orbital is stabilized in **C3** compared to **C1** (SOMO: **C1** (−4.74 eV), **C2** (−4.84 eV), **C3** (−4.93 eV)) (Fig S17, ESI†). This decreases the energy gap between the SOMO → SOMO−1 transition in **C3** and matches with the triplet-singlet energy gap of O$_2$. Thus, the enhanced S1 → T1 ISC increases the singlet oxygen quantum yield of **C3**, lowering the fluorescence quantum yield.
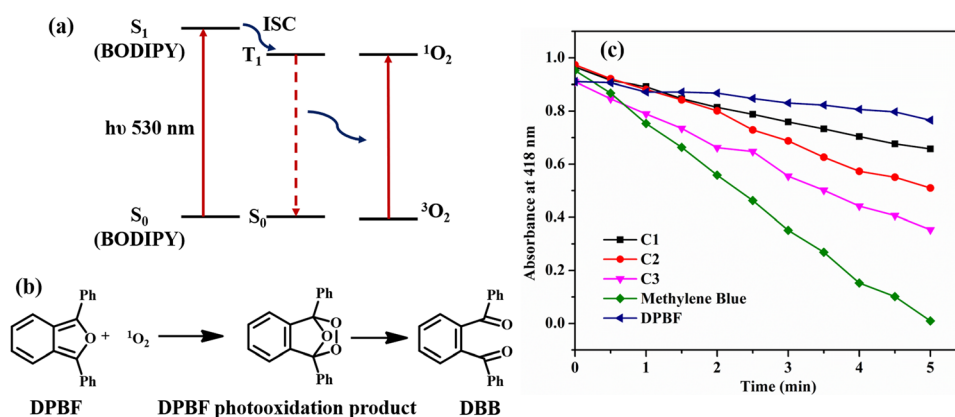


**Fig. 9** (a) The mechanism of generation of singlet oxygen by brominated BODIPYs and (b) the degradation of DPBF in the presence of $^1O_2$; (c) the plot of DPBF absorbance at 418 nm *vs.* irradiation time in the presence of *meso*-carbazole substituted BODIPY **C1**, and the brominated derivatives **C2** and **C3**.

## Vapochromism

The vapour stimuli-responsive materials find applications in the detection of volatile organic compounds and the development of cost-effective and metal-free vapochromic organic materials is in great demand. We studied the vapochromic behavior of synthesized *meso*-carbazole BODIPY by exposing it to different volatile solvent vapors. The solvents of different polarities are taken in a screw-capped vial, and Whatman filter ($10^{-5}$ M) paper coated with BODIPY is placed inside the cap. The vial is heated, and the color change is observed under a UV lamp (Fig. 10). The BODIPY **C1** has a red-shifted emission as the solvent polarity is increased, and the emission color observed on the filter paper is at par with the solvatochromic behavior observed in the solution phase.

The green emission in toluene changes to red emission in DCM, which is quenched in more polar solvent methanol (Fig. 10). This is because the intramolecular charge transfer in the molecule is activated in the presence of solvent vapor, which in turn results in the emission property. The original color is restored within seconds as the solvent is removed from the filter paper. Similar behavior was observed in mono-bromo derivative **C2**, while dibromo derivative **C3** does not show any emission when stimulated by solvent vapor. The promising vaporesponsive property of *meso*-carbazole BODIPY **C1** and **C2** in the solid state can be utilized to develop sensors for volatile organic solvents.

## Aggregation-induced emission studies on *meso*-carbazole BODIPY

Considering the high solid fluorescence of the *meso*-carbazole substituted BODIPYs (Fig. S5c, ESI†), we studied the AIE



**Fig. 10** The luminescence of BODIPY **C1** on Whatman filter paper exposed to various solvent vapors taken under a UV lamp.
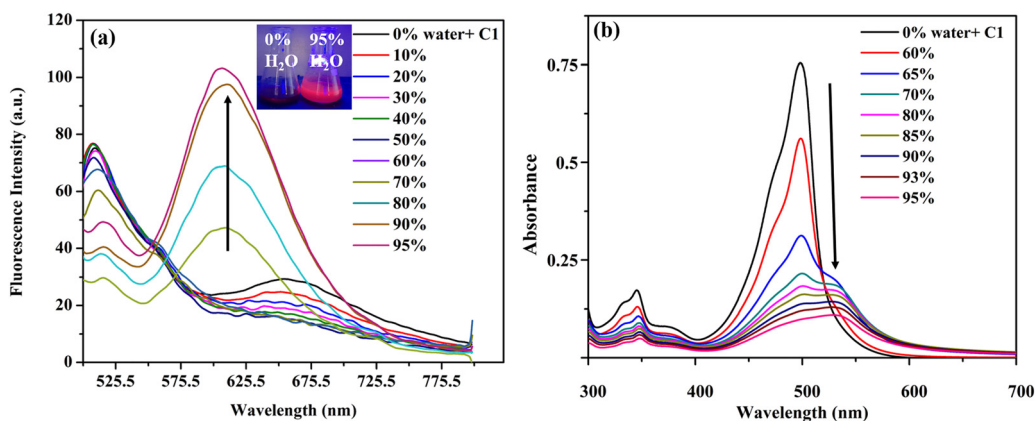
behavior of the dyes in the DMSO–water system, with different fractions of water ($f_w$) as an antisolvent. The dyes **C1**, **C2**, and **C3** are non-emissive in DMSO ($\Phi_f$: **C1** = 0.02, **C2** = 0.01, **C3** = 0.001) due to the TICT effect.

As discussed above, in pure DMSO, **C1** emits at 510 nm with TICT emission at 675 nm. As the amount of water in the DMSO increases, the TICT emission intensity at 675 nm decreases due to the further increase in the solvent polarity. When the water fraction increases to 70%, the formation of nano aggregates starts, and the aggregates exist in a less polar medium. This causes a blue shift in the TICT emission from 675 nm to 618 nm, along with an enhancement in emission efficiency, due to the restriction in intramolecular rotation of **C1** in the aggregates (Fig. 11a).

When the $f_w$ in the DMSO solution reached 95%, the emission intensity of the dye at 618 nm was approximately 5-fold higher than that in pure DMSO, and a strong red fluorescence was observed under UV light (Fig. 11b).

The AIE characteristics of brominated BODIPY **C2** in DMSO/H₂O mixtures were similar to those of **C1** (Fig. S18b, ESI†). The dibromo derivative **C3**, on the contrary, shows less enhancement in the fluorescence intensity at 630 nm, still, the solution is luminescent (Fig. S19b, ESI†). The quantitative enhancement of emission was estimated from the AIE factor ($\alpha_{AIE}$) (Table S9, ESI†). The AIE factor is calculated by comparing the quantum yields in solution and the aggregated state ($\Phi_f$ when $f_w$ = 95%: **C1** = 0.52, **C2** = 0.21, **C3** = 0.015) and is found to be 26, 21, and 15, respectively, for **C1**, **C2**, and **C3**. This indicates that the *meso*-carbazole substituted BODIPYs, **C1**, **C2**, and **C3**, are AIE-active, being non-fluorescent in solution, and emitting intensely in their aggregated state.

The formation of nano-aggregates was confirmed by absorption spectral studies. It was observed that the absorption peak of **C1** was slightly red-shifted and broadened from 499 nm to 527 nm as $f_w$ increased from 0% to 95% (Fig. 11b). There is a regular decrease in the absorbance along with the disappearance of the fine structure, due to the decrease in the concentration of DMSO solution of BODIPY and the formation of



**Fig. 11** (a) Fluorescence spectra of **C1** in DMSO–H₂O mixtures with different water fractions ($10^{-6}$ M, $\lambda_{exc}$ = 490 nm) (inset: photograph of **C1** in DMSO/H₂O mixture ($f_w$ = 0% and 95%), taken under 365 nm excitation of a UV lamp; (b) absorption spectra of **C1** in DMSO–H₂O mixtures with different water fractions ($10^{-5}$ M).

nano-aggregates. A levelling-off tail is observed in the longer wavelength region of the absorption spectra. This is because of the decrease in the light transmission of the mixture due to the light scattering of the nanoaggregate suspensions in the aqueous mixture (Mie effect).[48] This is direct evidence of particle formation. Although similar spectral changes are observed for BODIPYs **C2** and **C3**, the red shift in the absorption spectra is not very significant (Fig. S18a and S19a, ESI†).

The size, shape, and morphology of the aggregates formed with the increase in water fraction were studied using DLS and SEM analyses. In the aqueous mixture of **C1** with 70% water, aggregates with an average diameter of 157 nm are formed (Fig. S20, ESI†).

The brominated derivatives **C2** and **C3** form aggregates with average diameters of 201 nm and 217 nm, respectively. The SEM images of the compounds obtained by drop-casting 7:3 water–DMSO mixtures gave a clear representation of the morphology of the aggregates at the onset of aggregation. The BODIPY **C1** assembled into belt-like nanostructures, while **C2** had a flower-shaped crystalline structure. Also, aggregates of **C3** were structurally spherical at 70% water (Fig. 12).

**Single crystal structure analysis and theoretical calculations**

The single-crystal XRD analysis explains the packing of the molecules during aggregation (Fig. 1). The molecules of BODIPY **C1** have a twisted conformation, which effectively inhibits the emission quenching caused by the unfavorable $\pi$–$\pi$ interactions between the dye molecules. As discussed earlier, the packing is stabilized by multiple B$\cdots$H(carbazole), (Pyr)C$\cdots$C(carbazole) interactions and C–H$\cdots$F hydrogen bonding interactions between the adjacent molecules. These multiple noncovalent interactions rigidify the molecular conformation in the aggregate state and restrict the intramolecular rotation of the carbazole unit, allowing the BODIPYs to emit strongly.

To better understand the optical behavior of the dye aggregates, we calculated the rotational energy. As discussed earlier, the free rotation of the carbazole concerning the BODIPY core around the single bond is possible in an isolated molecule as it easily overcomes the barrier of 1.46 kcal mol$^{-1}$ at room temperature. This free rotation is restricted upon aggregation resulting in enhanced emission (Fig. S21, ESI†). The stable geometry has the dihedral angle $-51.1°$, $51.1°$, and $128.8°$ between the planes of carbazole and BODIPY. We measured
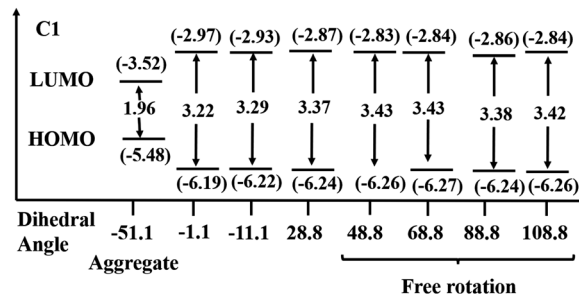


**Fig. 13** HOMO–LUMO energy gap in **C1** at different dihedral angles at the BP86/Def2-TZVPP level of theory. Eigenvalues are given in eV.

the HOMO–LUMO energy gap at different dihedral angles and found it to be less when the dihedral angle is $-51.1°$ (which is a conformation similar to the crystal structure), compared to other dihedral angles at which the carbazole unit has a free rotation (Fig. 13). Thus, the HOMO–LUMO gap decreases and nearly overlaps in the aggregates, generating a radiative emission pathway and producing a bright red fluorescence.

**Antileishmanial studies**

The inhibitory activity of the *meso*-carbazole substituted BODIPYs on the promastigotes of *Leishmania donovani* was carried out using the MTT assay. The promastigote form was chosen since it is the active form of the parasite observed in the human host. The IC$_{50}$ was calculated by plotting the concentration of the compounds *versus* the percentage viability, as shown in Fig. 14. The detailed methodology for the anti-leishmanial study is given in the experimental section (*vide infra*).

Interestingly, all the synthesized carbazole derivative BODIPYs exhibited anti-leishmanial activity against *Leishmania* promastigotes, and BODIPY **C2** has the highest activity. The IC$_{50}$ values of the compounds **C1, C2,** and **C3** were found to be 9.309 ± 2.567 µg mL$^{-1}$, 1.963 ± 0.272 µg mL$^{-1}$, and 9.285 ± 1.728 µg mL$^{-1}$ respectively and following the order **C1–C3** > **C2**. The IC$_{50}$ value of **C2** is very low compared to the carbazole (**C4**), which has an IC$_{50}$ value of 11.28 ± 1.791 µg mL$^{-1}$. It is understood from the anti-leishmanial assay that the compounds **C1–C3** exhibit increased activity, while the parent compound **C4**, from which the compounds **C1–C3** were derived, had lower activity.
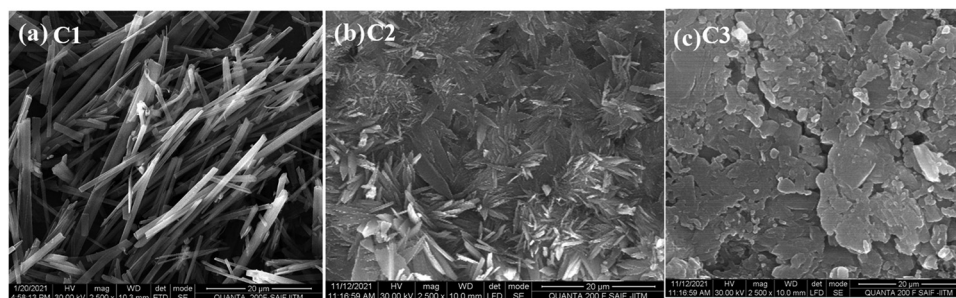


**Fig. 12** SEM images of *meso*-carbazole substituted BODIPYs ($10^{-5}$ M) in DMSO–water mixtures (30/70 v/v): (a) **C1**; (b) **C2**; (c) **C3**; magnification: 2.5k, scale bar: 20 µm.
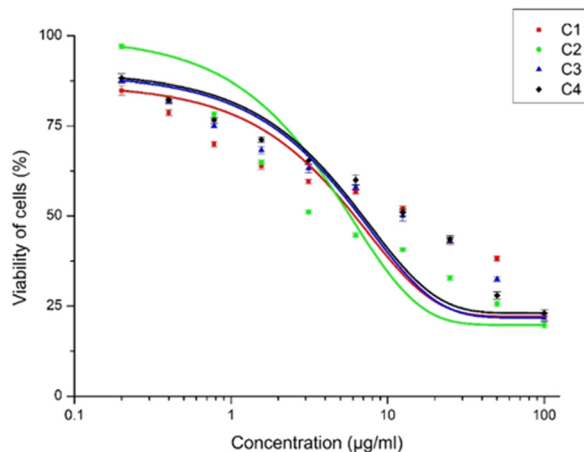
Fig. 14 The percentage viability of *Leishmania* promastigotes for different concentrations of compounds **C1**, **C2**, **C3**, and **C4** (0.2–100 μg mL$^{-1}$). **C4** is the electron-rich carbazole compound. The symbols represent the mean of three independent experiments and the error bars give the standard error of the mean. The higher activity of the **C2** compound relative to **C1** and **C3** can be clearly observed in the drug–response curves.

While **C2** with a mono-bromine substitution at the *meso*-position has higher activity, the dibromo derivative did not show an additive effect and rather had activity similar to **C1**. Therefore, the **C2** compound had the optimal functional groups at the desired positions that can bring about the necessary activity against the promastigotes of *Leishmania*. It has been reported earlier that a carbazole alkaloid, mahanine, induces ROS-mediated apoptosis in *Leishmania donovani* promastigotes.[36] We hypothesize that a similar mechanism of action might be the cause of the viability reduction of **C1**–**C3** compounds.

Contrary to our expectations, there was no change in the anti-leishmanial activity of the compounds in the presence of light. A possible reason for this might be the BODIPY moiety in the compounds that do not essentially contribute to the anti-leishmanial activity. It has been reported earlier that BODIPY compounds do not exhibit any anti-leishmanial activity but are able to maintain the activity of the anti-leishmanial miltefosine compound.[60] Similarly, our studies indicate that the activity of the compounds **C1**–**C3** is not derived exclusively from the BODIPY moiety alone but is a combinatorial effect of the carbazole, BODIPY and bromine substitutions. From the current study, these carbazole-derived compounds with mono and disubstituted Br groups at the *meso*-position have significant anti-leishmanial activity and can be taken forward as potential anti-leishmanial compounds.

## Conclusions

In summary, *meso*-carbazole substituted BODIPY (**C1**), and its brominated derivatives (**C2** and **C3**) were facilely synthesized. Carbazole substitution on the *meso*-position of the BODIPY core does not alter the energy levels of the π-conjugated system; however, the bromine substitution at the pyrrole carbon

produces a red-shift in the absorption and emission spectra. The BODIPYs **C1** and **C2** display a prominent solvatofluoro-chromic effect. Their emission is tuned in the entire visible region with a large Stokes shift due to the TICT effect. The fluorescence emission and solvatochromism are not prominent in the dibromo BODIPY derivative **C3** due to the heavy atom effect of bromine. Supportive evidence for enhanced ISC was obtained from the DPBF titration profiles and the molecular orbital analysis. Moreover, the synthesized compounds are strongly luminescent in aggregates. Increasing solvent polarity causes a large bathochromic shift in the emission. However, there is a dramatic decrease in the emission efficiency, and the red emission is greatly improved by aggregate formation. Thus, the AIE can enhance the TICT-induced red emission. Also, we propose the application of these compounds as a potential antileishmanial agent.

## Experimental section

### Materials and methods

Reagent-grade chemicals were used for the synthesis of all compounds. Pyrrole and boron trifluoride etherate (BF$_3$OEt$_2$) were purchased from Spectrochem (India) and were purified by passing through neutral alumina before use. N-Ethyl carbazole-3-carboxaldehyde purchased from TCI Chemicals (India) Pvt. Ltd and 2,3-dichloro-5,6-dicyano-*p*-benzoquinone (DDQ) obtained from Sigma Aldrich were used as received. Trifluor-oacetic acid (TFA) was purchased from Merck (India) and was distilled over P$_2$O$_5$. Triethylamine (Et$_3$N) purchased from Quali-gens was used as received. N-Bromosuccinimide (NBS) was purchased from Merck (India) and dried at 80 °C for 6 h after recrystallizing from hot water. Dimethylsulphoxide (DMSO), dimethylformamide (DMF), toluene, and acetonitrile were pur-chased from Fischer Scientific and were used as received. Chloroform, dichloromethane, hexane, and ethyl acetate were purchased from Avra Synthesis Pvt. Ltd. And were purified by distilling over K$_2$CO$_3$. Column chromatography was performed on silica gel (230–400 mesh) obtained from Avra.

FTIR data were collected on a JASCO FT/IR-4700 with KBr pellets. $^1$H and $^{13}$C NMR spectra were recorded with a Bruker 400 MHz FT-NMR spectrometer and Bruker AVIII 500 MHz FT NMR Spectrometer in CDCl$_3$ using TMS as the internal reference. UV-visible spectra were recorded on a JASCO V-750 instrument using quartz cuvettes at room temperature. Fluores-cence spectra were recorded on a PerkinElmer LS-55/Perkin-Elmer LS-45 luminescence spectrophotometer with a slit width of 15. High-Resolution MS data were recorded on a Shimadzu model 8045 LC-Q-TOF mass spectrometer. X-Ray diffraction data for **C1** were collected on a Bruker Kappa APEXII diffracto-meter. The fluorescence lifetime is measured using JOBIN-VYON M/S with Pulsed-Diode excitation sources using the TCSPC method ($\lambda_{exc}$ = 460 nm). SEM images are obtained using an FEI-Quanta FEG high-resolution scanning electron micro-scope. DLS measurements were done on the HORIBA SZ-100 nanoparticle analyzer. The DPBF titrations were carried out

using a light source of $\lambda$ = 400–750 nm, 15 J cm$^{-2}$ from Marutek.

## Synthesis of *meso*-carbazole BODIPY (C1)

*meso*-Carbazole substituted BODIPY was synthesized in a one-pot reaction, as described in Scheme 1, starting from acid-catalyzed condensation of N-ethyl carbazole-3-carboxaldehyde and pyrrole. To the N-ethyl carbazole-3-carboxaldehyde (1 equiv.), freshly distilled pyrrole (20 equiv.) and a catalytic amount of trifluoroacetic acid (TFA) were added under a N$_2$ atmosphere. Upon completion of the reaction in 30 minutes, the excess pyrrole is removed. The corresponding dipyrromethane (100 mg, 2 mmol) in DCM is immediately treated with an equimolar amount of 3-dichloro-5,6-dicyano-1,4-benzoquinone (DDQ) (75 mg, 2 mmol) under nitrogen atmosphere for 1 h at room temperature. TLC indicated the formation of dipyrromethene, which was further treated with triethylamine (5 mL) and complexed with borontrifluoroetherate (5 mL) in DCM for 30–45 minutes. The crude product was then washed with water, extracted with CHCl$_3$, filtered, and the solvent was removed under reduced pressure. This was further purified by silica gel column chromatography using chloroform/hexane (8 : 2) to afford an orange-red powder.

## Synthesis of brominated BODIPYs (C2 and C3)

To the solution of BODIPY (200 mg, 0.0052 moles) dissolved in dry DCM, 2.4 equivalents of recrystallized *N*-bromosuccinimide (NBS) (184 mg, 0.00156 moles) in dry DCM were added dropwise and stirred at room temperature for about 15 hours for the completion of the reaction. The reaction mixture was washed with water, extracted with chloroform, and evaporated. The purification was performed by column chromatography on silica gel using CHCl$_3$/hexane as eluent, which gave two products, mono-brominated (C2) and di-brominated (C3) derivatives, along with a minor amount of unreacted BODIPY C1.

**4,4-Difluoro-8-(*N*-ethyl carbazole)-4-bora-3a,4a-diaza-s-indacene (C1).** Purified by silica gel column chromatography, CHCl$_3$/hexane (80/20), reddish fluorescent dye. Yield = 35%. UV/vis (CHCl$_3$): $\lambda_{\max}$ (log $\varepsilon$) = 498 nm (4.42); fluorescence (CHCl$_3$): $\lambda_{em}$ = 578 nm ($\lambda_{exc}$ = 490 nm). $^1$H NMR (500 MHz, CDCl$_3$, $\delta$ in ppm): 1.52 (t, 3H, –CH$_3$), 4.46 (q, 2H, –CH$_2$), 6.57 (d, 2H, Py-H), 7.04 (d, 2H, Py-H), 7.94 (s, 2H, Py-H), 8.35 (s, 1H, Ar-H), 8.14 (d, 1H, Ar-H), 7.73 (m, 2H, Ar-H), 7.53 (d, 2H, Ar-H), 7.71 (d, 1H, Ar-H). $^{13}$C NMR (125 MHz, CDCl$_3$, $\delta$ in ppm): $\delta$ 146.1, 145.2, 141.1, 136.4, 133.3, 134.3, 132.2, 130.16, 130.4, 131.3, 129.6, 120.61, 110.2, 106.9, 39.5, 14.1. IR (KBr, cm$^{-1}$): 2922, 2364, 1596, 1531, 1380, 1257, 1068, 983, 770. HRMS (ESI-TOF) *m/z* [M + H]$^+$: 385.1573 (calc. = 384.1495).

**2-Bromo-4,4-difluoro-8-(*N*-ethyl carbazole)-4-bora-3a,4a-diaza-s-indacene (C2).** Purified by silica gel column chromatography, CHCl$_3$/hexane (60/40), Orange solid. Yield = 75%. UV/vis (CHCl$_3$): $\lambda_{\max}$ (log $\varepsilon$) = 515 nm (4.24); fluorescence (CHCl$_3$): $\lambda_{em}$ = 587 nm ($\lambda_{exc}$ = 490 nm). $^1$H NMR (500 MHz, CDCl$_3$, $\delta$ in ppm): 1.52 (t, 3H, –CH$_3$), 4.46 (q, 2H, –CH$_2$), 6.63 (s, 1H, Py-H), 6.97 (s, 1H, Py-H), 7.07 (s, 1H, Py-H), 7.38 (m, 1H, Ar-H), 7.53 (m, 1H, Ar-H), 7.63 (d, 1H, Ar-H), 7.69 (d, 1H, Ar-H), 7.79 (s, 1H, Ar-H), 8.00 (s, 1H, Py-H), 8.19

(d, 1H, Ar-H), 8.26 (s, 1H, Py-H), 8.33 (s, 1H, Ar-H). $^{13}$C NMR (125 MHz, CDCl$_3$, $\delta$ in ppm): $\delta$ 148.1, 147.2, 143.1, 136.4, 135.3, 134.3–134.2, 132.16, 131.4, 131.3, 129.6, 120.61, 106.9, 39.5, 14.1. IR (KBr, cm$^{-1}$): 2913, 2350, 1745, 1551, 1465, 1366, 1224, 1087, 988, 818, 718, 576. HRMS (ESI-TOF) *m/z* [M]$^+$: 465.0664 (calc. = 465.0623).

**2,6-Dibromo-4,4-difluoro-8-(*N*-ethyl carbazole)-4-bora-3a,4a-diaza-s-indacene (C3).** Purified by silica-gel column chromatography, CHCl$_3$/hexane (60/40), Pink solid. Yield = 25%. UV/vis (CHCl$_3$): $\lambda_{\max}$ (log $\varepsilon$) = 534 nm (4.32); fluorescence (CHCl$_3$): $\lambda_{em}$ = 551 nm ($\lambda_{exc}$ = 490 nm). $^1$H NMR (500 MHz, CHCl$_3$, $\delta$ in ppm): 1.57 (3H, d, –CH$_3$), 4.56 (2H, q, –CH$_2$), 7.55 (2H, m, Ar-H), 7.61 (1H, m, Ar-H), 8.32 (1H, s, Ar-H), 8.19 (1H, d, Ar-H), 7.84 (2H, s, Py-H), 8.39 (2H, d, Py-H), 7.69 (1H, d, Ar-H). $^{13}$C NMR (125 MHz, CDCl$_3$, $\delta$ in ppm): 145.5, 143.7, 141.7, 133.3, 132.1, 131.2, 128.4–128.3, 123.6, 117.3, 103.7, 38.2, 15.2. IR (KBr, cm$^{-1}$): 2926, 2355, 1730, 1541, 1466, 1367, 1262, 1122, 983, 578. HRMS (ESI-TOF) *m/z* [M + H]$^+$: 542.9751 (calc. = 541.9681).

## Measurement of fluorescent quantum yield

The fluorescence quantum yield ($\Phi_f$) is measured using the equation given below:

$$\Phi_f = \Phi_f^{ref} \frac{F_S A_R \eta_S^2}{F_R A_S \eta_R^2}$$

where $F_S$ and $F_R$ are the integrated fluorescence intensities of the sample and reference, $A_S$ and $A_R$ are the absorbances of the sample and reference at the excitation wavelength, and $\eta_S$ and $\eta_R$ are the refractive indices of the solvents used for the sample and reference. Fluorescein in 0.1 M NaOH solution was used as the reference ($\Phi_f^{ref}$ = 0.90, $\lambda_{ex}$ = 480 nm).

## Measurement of singlet oxygen quantum yield ($\Phi_\Delta$)

The singlet oxygen ($^1$O$_2$) acceptor, DPBF (1,3-diphenylisobenzofuran), (4.9 × 10$^{-5}$ M) with and without BODIPYs (10$^{-5}$ M) in DMSO was prepared in the dark and was irradiated using the light source of $\lambda$ > 450 nm at room temperature under stirring. The singlet oxygen generated by BODIPYs degrades the DPBF to 1,2-dibenzoylbenzene (DBB). At regular irradiation intervals, the degradation of the DPBF molecules was monitored by measuring the decrease in absorbance at 418 nm. A plot of absorption maxima of DPBF at 418 nm vs irradiation time is drawn. The singlet oxygen quantum yield is calculated using the equation given below:

$$\Phi_\Delta = \Phi_\Delta^{ref} \frac{k}{k^{ref}} \frac{I^{ref}}{I}$$

where $k$ and $k^{ref}$ are the DPBF photo-bleaching rate constants in the presence of the samples and reference, respectively, which are obtained from the slope of the plot of irradiation time *vs.* absorption maxima of DPBF at 418 nm; $I$ and $I^{ref}$ are the rates of light absorption at the irradiation wavelength by the samples and reference, respectively. Methylene blue was used as the reference ($\Phi_\Delta$ = 0.52).

### Preparation of aggregates

The stock solution of the compounds was prepared in DMSO ($10^{-3}$ M). The portions of stock solution were pipetted out into a vial, along with an adequate amount of water (0–95%) under vigorous stirring to furnish $10^{-5}$ M solutions. The UV-vis and fluorescence measurements of the freshly prepared solutions were performed.

### Computational methodology

The quantum mechanical calculations were carried out with the Gaussian 09[52] software package. The ground-state geometry optimizations were performed at the DFT[50] level of theory using the exchange of Becke in conjunction with the correlation functional of Perdew (BP86).[51] The basis set used is def2-TZVPP.[54] The single-point calculations on the resulting optimized geometries have also been carried out using meta-GGA exchange–correlation functional M06[53] with the Def2-TZVPP basis set. The electronic energy from the single point calculation at the M06/Def2-TZVPP level of theory and the zero-point correction at the BP86/Def2-TZVPP level of theory are summed to obtain the total electronic energy of the molecule. The molecular electrostatic potential (MESP) maps were calculated on the van der Waals surface at the same level of theory and analyzed using the Multiwfn software package.[57] The time-dependent density functional theory (TDDFT)[55] calculations were performed at the M06/Def2-TZVPP level of the Gaussian 09 program using the PCM model[56] in DMSO.

### Antileishmanial studies: methodology

The antileishmanial activity of the compounds **C1**, **C2**, **C3**, and **C4** (carbazole) was investigated by an MTT cell proliferation assay.[59] The assay is based on the colorimetric deduction of the reduced product of MTT [3-(4,5-dimethylthiazol-2-yl)-2,5-diphenyltetrazolium bromide] dye. The reduction is caused by various enzymes in the mitochondria wherein the tetrazolium dye is converted into purple insoluble formazan crystals in viable cells. Initially, the compounds were serially diluted in a concentration range from 0.2–100 µg mL$^{-1}$ to a total volume of 100 µL in a 96 well culture plate. To this, exponential growth phase promastigote cells ($1 \times 10^6$ cell mL$^{-1}$) grown in RPMI-1640 media supplemented with 15% FBS (Foetal Bovine Serum) were added to the 96 well culture plate and allowed to grow for 24 h at 25 °C. After the incubation, MTT was added to the 96-well culture plate and incubated in the dark for 4 h at 25 °C until the formation of insoluble formazan crystals. The insoluble formazan crystals were solubilized by the addition of 10% SDS and then incubated for 4 h. The absorbance was then measured at 570 nm using a 96-well plate reader. The calculated IC$_{50}$ is the concentration of the compounds required for a 50% reduction in cell viability.

## Conflicts of interest

There are no conflicts to declare.

## Acknowledgements

## References

1 K. V. Rao, A. Jain and S. J. George, *J. Mater. Chem. C*, 2014, **2**, 3055–3064.

2 A. Maity, A. Sarkar, S. Bhaktha and S. K. Patra, *New J. Chem.*, 2020, **44**, 14650–14661.

3 K. P. Carter, A. M. Young and A. E. Palmer, *Chem. Rev.*, 2014, **114**, 4564–4601.

4 T. T. Divya, D. Raghav, K. Rathinasamy and L. Chakkumkumarath, *New J. Chem.*, 2019, **43**, 16349–16358.

5 Y. Ni and J. Wu, *Org. Biomol. Chem.*, 2014, **12**, 3774–3791.

6 A. Brzeczek, K. Piwowar, W. Domagala, M. M. Mikołajczyk, K. Walczak and P. Wagner, *RSC Adv.*, 2016, **6**, 36500–36509.

7 P. Rybczynski and A. Kaczmarek-Kedziera, *Struct. Chem.*, 2021, **32**, 953–965.

8 L. Jiao, W. Pang, J. Zhou, Y. Wei, X. Mu, G. Bai and E. Hao, *J. Org. Chem.*, 2011, **76**, 9988–9996.

9 M. Obłoza, Ł. Łapok, T. Pędziński and M. Nowakowska, *Asian J. Org. Chem.*, 2019, **8**, 1879–1892.

10 V. Lakshmi and M. Ravikanth, *Dalton Trans.*, 2012, **41**, 5903–5911.

11 D. Prasannan, D. Raghav, S. Sujatha, H. Hareendrakrishna Kumar, K. Rathinasamy and C. Arunkumar, *RSC Adv.*, 2016, **6**, 80808–80824.

12 R. Prieto-Montero, A. Prieto-Castaneda, R. Sola-Llano, A. R. Agarrabeitia, D. García-Fresnadillo, I. Lopez-Arbeloa, A. Villanueva, M. J. Ortiz, S. Moya and V. Martınez-Martınez, *Photochem. Photobiol.*, 2020, **96**, 458–477.

13 Y. Gawale and N. Sekar, *J. Photochem. Photobiol. B: Biol.*, 2018, **178**, 472–480.

14 H. Wang, E. Zhao, J. W. Y. Lam and B. Z. Tang, *Mater. Today*, 2015, **18**, 365–377.

15 J. Mei, N. L. Leung, R. T. Kwok, J. W. Lam and B. Z. Tang, *Chem. Rev.*, 2015, **115**, 11718–11940.

16 E. Li, K. Jie, M. Liu, X. Sheng, W. Zhu and F. Huang, *Chem. Soc. Rev.*, 2020, **49**, 1517–1544.

17 O. S. Wenger, *Chem. Rev.*, 2013, **113**, 3686–3733.

18 S. Yokoyama, H. Asahara and N. Nishiwaki, *Cryst. Growth Des.*, 2020, **20**, 1383–1387.

19 Y. Li, J. Ding, M. Day, Y. Tao, J. Lu and M. D'iorio, *Chem. Mater.*, 2004, **16**, 2165–2173.

20 M. S. Mudadu, A. N. Singh and R. P. Thummel, *J. Org. Chem.*, 2008, **73**, 6513–6520.

21 P. E. Kesavan and I. Gupta, *Dalton Trans.*, 2014, **43**, 12405–12413.

22 V. Promarak, M. Ichikawa, T. Sudyoadsuk, S. Saengsuwan, S. Jungsuttiwong and T. Keawin, *Thin Films*, 2008, **516**, 2881–2888.

23 Z.-S. Wang, N. Koumura, Y. Cui, M. Takahashi, H. Sekiguchi, A. Mori, T. Kubo, A. Furube and K. Hara, *Chem. Mater.*, 2008, **20**, 3993–4003.

24 A. Głuszyńska, *Eur. J. Med. Chem.*, 2015, **94**, 405–426.

25 G. Reddy, N. Duvva, S. Seetharaman, F. D'Souza and L. Giribabu, *Phys. Chem. Chem. Phys.*, 2018, **20**, 27418–27428.

26 S. Wanwong, P. Khomein and S. Thayumanavan, *Chem. Cent. J.*, 2018, **12**, 60–69.

27 D. Zhang, Y. Wang, Y. Xiao, S. Qian and X. Qian, *Tetrahedron*, 2009, **65**, 8099–8103.

28 I. Gupta and P. E. Kesavan, *Front. Chem.*, 2019, **7**, 841–872.

29 H. Y. Lin, W. C. Huang, Y. C. Chen, H. H. Chou, C. Y. Hsu, J. T. Lin and H.-W. Lin, *Chem. Commun.*, 2012, **48**, 8913–8915.

30 P. Yang, W. Wu, J. Zhao, D. Huang and X. Yi, *J. Mater. Chem.*, 2012, **22**, 20273–20283.

31 Y. Ooyama, M. Kanda, T. Enoki, Y. Adachi and J. Ohshita, *RSC Adv.*, 2017, **7**, 13072–13081.

32 J. Strahan, B. C. Popere, P. Khomein, C. A. Pointer, S. M. Martin, A. N. Oldacre, S. Thayumanavan and E. R. Young, *Dalton Trans.*, 2019, **48**, 8488–8501.

33 X. Xia and Y. Qian, *Analyst*, 2018, **143**, 5218–5224.

34 R. Misra, T. Jadhav, B. Dhokale, P. Gautam, R. Sharma, R. Maragani and S. M. Mobin, *Dalton Trans.*, 2014, **43**, 13076–13086.

35 J. J. Brendle, A. Outlaw, A. Kumar, D. W. Boykin, D. A. Patrick, R. R. Tidwell and K. A. Werbovetz, *Antimicrob. Agents Chemother.*, 2002, **46**, 797–807.

36 S. Roy, D. Dutta, E. M. Satyavarapu, P. K. Yadav, C. Mandal, S. Kar and C. Mandal, *Sci. Rep.*, 2017, **7**, 4141–4148.

37 S. M. Thomas, A. Purmal, M. Pollastri and K. Mensa-Wilmot, *Sci. Rep.*, 2016, **6**, 32083–32093.

38 I. F. Sengul, E. Okutan, H. Kandemir, E. Astar and B. Çosut, *Dyes Pigm.*, 2015, **123**, 32–38.

39 Y. Hayashi, S. Yamaguchi, W. Y. Cha, D. Kim and H. Shinokubo, *Org. Lett.*, 2011, **13**, 2992–2995.

40 V. Lakshmi, M. R. Rao and M. Ravikanth, *Org. Biomol. Chem.*, 2015, **13**, 2501–2517.

41 Y. J. Chen, Y. Ling, L. Ding, C. L. Xiang and G. Zhou, *J. Mater. Chem. C*, 2016, **4**, 8496–8505.

42 S. K. Saha, P. Purkayastha and A. B. Das, *J. Photochem. Photobiol., A*, 2008, **195**, 368–377.

43 (*a*) R. Hu, E. Lager, A. Aguilar-Aguilar, J. Liu, J. W. Y. Lam, H. H. Y. Sung, I. D. Williams, Y. Zhong, K. S. Wong, E. Pena-Cabrera and B. Z. Tang, *J. Phys. Chem. C*, 2009, **113**, 15845–15853; (*b*) A. Kundu, S. Karthikeyan, Y. Sagara, D. Moon and S. P. Anthony, *ACS Omega*, 2019, **4**, 5147–5154.

44 X.-F. Zhang and X. Yang, *J. Phys. Chem. B*, 2013, **117**, 5533–5539.

45 C. Wang and Y. Qian, *Org. Biomol. Chem.*, 2019, **17**, 8001–8007.

46 R. T. Kuznetsova, I. V. Aksenova, D. E. Bashkirtsev, A. S. Shulev, E. V. Antina, M. B. Berezin and N. A. Bumagina, *High Energy Chem.*, 2017, **51**, 175–181.

47 (*a*) V. E. Z. Lippert, *Elektrochem*, 1957, **61**, 962–975; (*b*) N. Mataga, Y. Kaifu and M. Koizumi, *Bull. Chem. Soc. Jpn.*, 1956, **29**, 465–470.

48 C. Y. K. Chan, J. W. Y. Lam, Z. Zhao, S. Chen, P. Lu, H. H. Y. Sung, H. S. Kwok, Y. Ma, I. D. Williams and B. Z. Tang, *J. Mater. Chem. C*, 2014, **2**, 4320–4327.

49 P. Das, A. Kumar, A. Chowdhury and P. S. Mukherjee, *ACS Omega*, 2018, **3**, 13757–13771.

50 (*a*) W. Kohn and L. J. Sham, *Phys. Rev.*, 1965, **140**, A1133–A1138; (*b*) P. J. Stephens, F. J. Devlin, C. F. Chabalowski and M. J. Frisch, *J. Phys. Chem.*, 1994, **98**, 11623–11627.

51 (*a*) A. D. Becke, *Phys. Rev. A*, 1988, **38**, 3098–3100; (*b*) J. P. Perdew, *Phys. Rev. B*, 1986, **33**, 8822–8824.

52 M. J. Frisch, G. W. Trucks, H. B. Schlegel, G. E. Scuseria, M. A. Robb, J. R. Cheeseman, G. Scalmani, V. Barone, G. A. Petersson, H. Nakatsuji, X. Li, M. Caricato, A. Marenich, J. Bloino, B. G. Janesko, R. Gomperts, B. Mennucci, H. P. Hratchian, J. V. Ortiz, A. F. Izmaylov, J. L. Sonnenberg, D. Williams-Young, F. Ding, F. Lipparini, F. Egidi, J. Goings, B. Peng, A. Petrone, T. Henderson, D. Ranasinghe, V. G. Zakrzewski, J. Gao, N. Rega, G. Zheng, W. Liang, M. Hada, M. Ehara, K. Toyota, R. Fukuda, J. Hasegawa, M. Ishida, T. Nakajima, Y. Honda, O. Kitao, H. Nakai, T. Vreven, K. Throssell, J. A. Montgomery, Jr., J. E. Peralta, F. Ogliaro, M. Bearpark, J. J. Heyd, E. Brothers, K. N. Kudin, V. N. Staroverov, T. Keith, R. Kobayashi, J. Normand, K. Raghavachari, A. Rendell, J. C. Burant, S. S. Iyengar, J. Tomasi, M. Cossi, J. M. Millam, M. Klene, C. Adamo, R. Cammi, J. W. Ochterski, R. L. Martin, K. Morokuma, O. Farkas, J. B. Foresman and D. J. Fox, *Gaussian 09, Revision A.02*, Gaussian, Inc., Wallingford CT, 2016.

53 Y. Zhao and D. G. Truhlar, *Theor. Chem. Acc.*, 2008, **120**, 215–241.

54 F. Weigend, M. Häser, H. Patzelt and R. Ahlrichs, *Chem. Phys. Lett.*, 1998, **294**, 143–152.

55 A. Dreuw and M. Head-Gordon, *Chem. Rev.*, 2005, **105**, 4009–4037.

56 M. R. P. Long and C. M. Isborn, *J. Phys. Chem. B*, 2017, **121**, 10105–10117.

57 (*a*) T. Lu and F. Chen, *J. Comput. Chem.*, 2012, **33**, 580–592; (*b*) T. Lu and F. Chen, *J. Mol. Graphics Modell.*, 2012, **38**, 314–323.

58 (*a*) Z. R. Grabowski and J. Dobkowski, *Pure & Appl. Chem.*, 1983, **55**, 245–252; (*b*) H. Sinha, S. Muralidharaan and K. Yates, *Can. J. Chem.*, 1992, **70**, 1932–1938; (*c*) C. Zhong, *Phys. Chem. Chem. Phys.*, 2015, **17**, 9248–9257.

59 S. Sasidharan and P. Saudagar, *Acta Trop.*, 2022, **231**, 106448.

60 V. Hornillos, E. Carrillo, L. Rivas, F. Amat-Guerri and A. U. Acuña, *Bioorg. Med. Chem.*, 2008, **18**, 6336–6339.

61 W. Hu, Y. Lin, X.-F. Zhang, M. Feng, S. Zhao and J. Zhang, *Dyes Pigm.*, 2019, **164**, 139–147.